Research Article

Nano Research
2021, 14(11): 4146–4153

ISSN 1998-0124 CN 11-5974/O4
https://doi.org/10.1007/s12274-021-3355-6

Achieving room-temperature M2-phase VO_2 nanowires for superior thermal actuation

Yong-Qiang Zhang[1,§], Kai Chen[1,§], Hao Shen[1], Yue-Cun Wang[1], Mohamed Nejib Hedhili[2], Xixiang Zhang[2], Ju Li[3] (✉), and Zhi-Wei Shan[1] (✉)

[1] *Center for Advancing Materials Performance from the Nanoscale, State Key Laboratory for Mechanical Behavior of Materials, Xi'an Jiaotong University, Xi'an 710049, China*

[2] *Physical Science and Engineering Division, King Abdullah University of Science and Technology (KAUST), Thuwal 23955-6900, Saudi Arabia*

[3] *Departments of Nuclear Science and Engineering and Materials Science and Engineering, Massachusetts Institute of Technology, Cambridge, MA 02139, USA*

[§] *Yong-Qiang Zhang and Kai Chen contributed equally to this work.*

Received: 24 September 2020 / **Revised:** 21 December 2020 / **Accepted:** 21 January 2021

ABSTRACT

Vanadium dioxide (VO_2) has emerged as a promising micro-actuator material for its large amplitude and high work density across the transition between the insulating (M1 and M2) and metallic (R) phase. Even though M2–R transition offers about 70% higher transformation stress than M1–R structural phase transition, the application of the M2 phase in the micro-actuators is hindered by the fact that previously, M2 phase can only stay stable under tensile stress. In this work, we propose and verify that by synthesizing the VO_2 nanowires under optimized oxygen-rich conditions, stoichiometry change can be introduced into the nanowires (NWs) which in turn yield a large number free-standing single-crystalline M2-phase NWs stable at room temperature. In addition, we demonstrate that the output stress of the M2-phase NWs is about 65% higher than that of the M1-phase NWs during their transition to R phase, quite close to the theoretical prediction. Our findings open new avenues towards enhancing the performance of VO_2-based actuators by using M2–R transition.

KEYWORDS

single crystalline vanadium dioxide (VO_2) nanowires, metal-insulator transition, room-temperature M2 phase, micro-actuator, martensitic transformation, transformation strain

1 Introduction

Micro-actuators with high actuation amplitude and high work are of vital importance for applications in microelectromechanical systems (MEMS), microrobotics, and medical devices [1–3]. Vanadium dioxide (VO_2) stands out among various competing actuation materials [4], benefitting from its high elastic modulus (~ 140 GPa) [5–7] and easy-to-access metal-insulator transition (MIT) at 68 °C [8, 9]. Across the MIT, the low-temperature insulating M1 or M2 phase transforms into the high-temperature R phase, accompanied with a significant lattice shrinkage (the so-called transformation strain) of 1% or higher along the *c*-axis of the R phase, which provides the driving force for the actuation. The transformation strain achieved is ~ 0.3% in the M1-phase polycrystalline VO_2-film-based bimorph structures [4, 10–13], and then promoted to ~ 1% by using the single-crystalline M1-phase nanowires (NWs), close to the theoretical value [14–16]. Higher actuation is possible by replacing the starting material with the M2-phase single crystals, which possess higher shrinkage transformation strain (~ 1.7%) than the M1 phase (~ 1%) [5, 9, 17] (Fig. 1).

However, room-temperature-stable stress-free single-crystalline M2-phase NWs are difficult to synthesize. Although M2-phase polycrystalline thin films and single-crystalline microbelts have been prepared by cation dopants with lower valence such as Al^{3+} and Cr^{3+} [18, 19], no success has been reported on uniform M2-phase NWs fabrication due to the unevenly distributed dopants and the consequent inhomogeneous phase distribution [20]. Alternatively, tuning the VO_2 stoichiometric ratio is also proposed to modulate the phase. Deduced from the phenomenon of Cr-doping, the increase of V^{5+}/V^{4+} ratio is believed to favor the formation of the M2 phase [11, 19, 21]. By introducing an oxidative atmosphere at the early stage of a multi-step growth process, M2-phase NWs are synthesized, although no direct stoichiometry evidence is provided [22]. It is noted that introducing oxygen in the growth process may easily turn the NWs into oxygen-excess phases (V_2O_5 and V_6O_{13} for example) [23] and lower the yield of M2 phase [24]. Furthermore, the actuation ability achieved by the room-temperature-stabilized M2-phase NWs is still unverified. As a result, a more reliable and high-yield strategy is needed to modulate the stoichiometry and phase of NWs, and their practical actuation ability needs to be quantified.

In this study, we synthesize the free-standing single-crystalline

Address correspondence to Zhi-Wei Shan, zwshan@mail.xjtu.edu.cn; Ju Li, liju@mit.edu

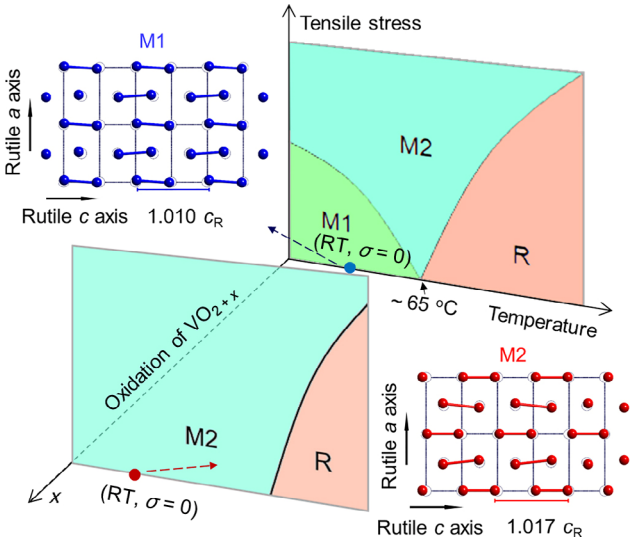

Figure 1 Estimated influence of vanadium deficiency in VO_{2+x} on the stress (uniaxial along c_R)-temperature phase diagram. The arrangements of vanadium ions in the M1, M2, and R phases viewing from the *b* axis of the R phase are shown, indicating the M2 phase possesses higher shrinkage transformation strain than the M1 phase across the MIT.

M2-phase VO_2 NWs stable at room temperature under a unique growth condition. High temperature and low Ar gas carrier flux are controlled to achieve rapid growth rate of NW, introduce oxygen interstitial growth defects [25, 26], modify the oxygen stoichiometry, and consequently modulate the phase. No extra oxygen is supplied intentionally during the whole synthetic process to successfully avoid the formation of other vanadium oxides. The oxidation states of the V cations are characterized and compared with the M1-phase NWs, proving the existence of off-stoichiometric defects. Furthermore, the superior actuation ability of the M2-phase NWs over the M1-phase NWs (~ 65% higher) is demonstrated quantitatively using the *in situ* transmission electron microscopy (TEM), revealed to be close to the theoretical prediction for the pristine M2 phase.

2 Results and discussions

Figure 1 schematically shows the idea of stabilizing the M2 phase to room temperature by tuning the oxygen deficiency. The oxygen deficiency-stress (uniaxial along c_R)-temperature phase diagram is adapted from the stress-temperature phase diagram of pure VO_2 [8, 9]. An extra axis of stoichiometric ratio (VO_{2+x}) is added representing the average valence of the V cations. As illustrated in Fig. 1, just the right amount of oxygen excess in VO_{2+x} is proposed to stabilize the M2 phase. Intuitively, the phase boundaries in the phase diagram shift as the valence of the V cations varies, similar to the phase modulation effects of temperature and stress. The stress and temperature axes are martensitic, while the VO_{2+x} axis, on the contrary, involves diffusive mass action in growth, strongly depending on the synthetic conditions such as the oxygen partial pressure and growth rate, which inspire this work. The VO_2 NWs are synthesized using the catalyst-free thermal evaporation approach [27], and the setup is displayed schematically in Fig. 2(a). For safety concern, VO_2 powder is employed as the source, to avoid the use of toxic V_2O_5. In significant contrast to previous study, the unpolished Si substrates, instead of being placed downstream in the carrying tube, are mounted about 5 mm right above the VO_2 source powder, where the temperature and vapor density are higher. The typical morphology and microstructure of the NWs grown at 1,000 °C with 50 sccm Ar flow rate are characterized with scanning electron microscope (SEM) and TEM, respectively. As shown in the SEM image in Fig. 2(b), the products are predominated by free-standing, non-epitaxially grown NWs. The dimensions of the NWs span a wide range of 5 to 60 μm in length and the aspect ratio ranges from 20 to 120 (Fig. S1 in the Electronic Supplementary Material (ESM)). The inset in Fig. 2(b) shows the NWs with rectangular cross-section possess smooth and well-faceted surface. From X-ray energy dispersive spectroscopy study (EDS, see Fig. S2 in the ESM), no impurity elements besides V and O are detected.

The existence of room-temperature-stabilized M2-phase NWs is proved by the crystal structure characterization with TEM as shown in Fig. 2(c). The uniform contrast in the bright-field image evidences high crystalline quality. In the corresponding selected area diffraction patterns (SADP) in the inset, the M2 phase is identified and distinguished from the M1 phase by the characteristic $\{110\}_{M2}$ and $\{200\}_{M2}$ diffraction spots which do not exist in the M1 phase (the differences between the SADP for the M2 and M1 phase are discussed in Fig. S3 in the ESM). The SADP does not change when the electron beam is moved

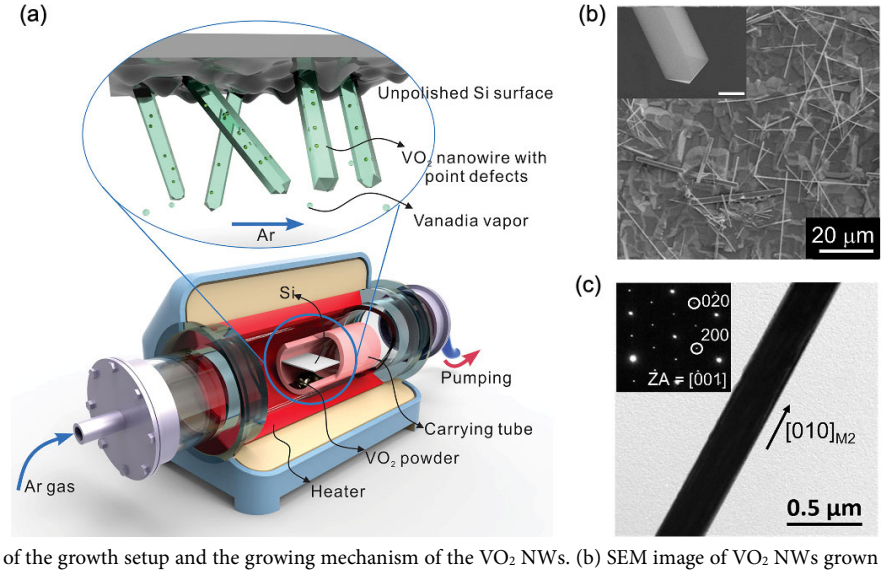

Figure 2 (a) Schematic of the growth setup and the growing mechanism of the VO_2 NWs. (b) SEM image of VO_2 NWs grown at 1,000 °C at 50 sccm Ar. Inset is a magnified SEM image showing the surface conditions of the individual NW. The scale bar in the inset is 500 nm. (c) TEM image of the individual M2-phase NW. Inset shows the corresponding SADP.

along the NW, indicating the NW is single-crystalline and single-phase. Analysis of the SADP from multiple individual NWs shows the M2-phase NW grows along $[010]_{M2}$, corresponding to the *c*-axis of the R phase [8, 9], in which direction the transformation strain is the largest.

The achievement of the free-standing M2-phase NWs is further confirmed with Raman spectroscopy. A micro-focused HeNe laser (λ = 632.8 nm) is employed, and the laser power is limited within 0.2 mW to minimize the sample heating. Figure 3(a) shows the typical Raman spectrum of the individual M2-phase (red) NW grown at 1,000 °C with 50 sccm Ar flow rate. The spectrum of the M1-phase (blue) NW is also shown for comparison. The M2 phase is identified by the dominant 654 cm^{-1} phonon frequency, agreeing with its C_{2h}^3 space group [28] and previous Raman measurements [29–31]. In contrast, the dominate peak of M1 phase appears at 610 cm^{-1}. No peaks related to other vanadium oxides such as V_2O_5 or V_6O_{13} [32] are observed. Raman mapping is conducted on individual M2-phase NWs to verify the phase distribution inside the NW. A series of Raman spectra along the NW are displayed in Fig. S4 in the ESM. The dominated peak appears at about 650 cm^{-1} in all spectra. Meanwhile, the feature peak for the M1 phase, which appears at about 610 cm^{-1}, is not observed, indicating the whole NW is in the M2 phase. By extracting the Raman intensity of the characteristic dominant peak at 650 cm^{-1}, the Raman image of the M2-phase NW is obtained and displayed in Fig. 3(b). The dimension and the boundary of the NW are clearly shown, which are consistent with the observation in the optical image in the inset. The contrast inside the NW is quite uniform, indicating the homogeneous Raman peak intensity and crystal structure. Raman mapping conducted on other NWs displayed in Fig. S5 in the ESM shows similar results. These Raman images prove that the whole M2-phase NWs are occupied by pure M2 phase, without M1-phase domains. Besides, the single-phase nature of the M2-phase NW is also supported by the results of uniaxial tensile test in the TEM (Fig. S6 in the ESM).

The yield of M2-phase NWs is sensitive to the growth temperature and Ar flow rate. Figures 3(c) and 3(d) show the population proportion of the M2-phase NWs under different growth temperatures and Ar flow rates. For each batch, about 20 individual single-phase single-crystalline NWs are randomly selected and their phase is identified one-by-one with micro-Raman spectroscope. It is clearly shown that the NWs obtained at 700 °C with the gas flow rate of 50 sccm are all in the M1 phase. With the increase of the growth temperature or the decrease of the gas flux, the yield of the M2 phase increases dramatically. The highest M2-phase fraction of 88% is obtained at 1,000 °C with gas flux of 50 sccm.

It is noticed that the oxidation states of the V cations in the NWs grown at different conditions are significantly different. X-ray photoelectron spectroscope (XPS) study is performed on the freshly prepared NWs grown at 1,000 °C with 50 sccm gas flux (M2 phase dominated, indicated by the red ball in Fig. 3(c)) and the M1-phase ones synthesized at 700 °C with 50 sccm gas flux (indicated by the blue ball in Fig. 3(c)), respectively. The sampling area is about 0.8 mm in diameter, thus a large number of NWs are probed in the measurements and the spectra represent the overall oxidation conditions of the NW surfaces. The experimentally collected XPS of these two samples are demonstrated as black dotted curves in Fig. 3(e). Sharp contrast is observed in terms of the position and shape of the core-level peaks ($2p_{3/2}$ and $2p_{1/2}$) of the V cations. The profile of these two peaks are fitted by the linear combination of V^{4+} and V^{5+} valence states, as illustrated by the orange and green curves, respectively. The summed intensity from these two valence states fits the experimental data well, as illustrated with the blue (M1 phase grown at 700 °C, upper panel) and red (M2 phase dominated grown at 1,000 °C, lower panel) curves, respectively. The V^{5+} peaks show up in both samples, indicating oxygen excess in the surface layers of both specimens, which has been discussed in the previous reports about VO_2 nanostructures [33]. The dominant contribution to the V $2p_{3/2}$ peak evolves from the V^{4+} peak in the M1-phase to the V^{5+} peak in the M2-phase dominated sample. The integrated intensity of the V^{5+} peak increases from 42% in the M1-phase sample

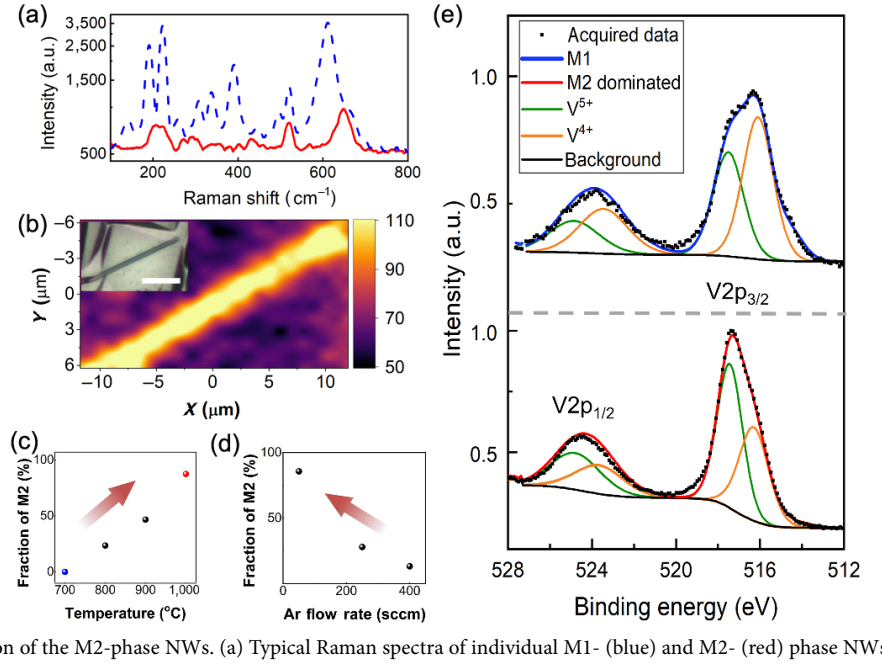

Figure 3 Characterization of the M2-phase NWs. (a) Typical Raman spectra of individual M1- (blue) and M2- (red) phase NWs. (b) Raman image of an individual M2-phase NW by extracting the intensity of the dominate peak at 650 cm^{-1}. Inset is the optical image of the NW. The scale bar is 5 μm. (c) and (d) show the dependence of the population proportion of the M2-phase on the growth temperature and Ar flow rate, respectively. The Ar flow rate is set to 50 sccm in (c), and the temperature is set to 1,000 °C in (d). (e) XPS show the valence states of the vanadium cations in the samples grown at 700 °C (the M1 phase, upper panel) and 1,000 °C (the M2 phase dominated, lower panel), respectively.

to 57% in the M2-dominated sample. Consequently, the stoichiometry is calculated to be $VO_{2.29}$ and $VO_{2.21}$ for the M2 and M1 phase, respectively (details are shown in Table S1 in the ESM). It is clear that the oxidation states of the V cations in the M2 phase are on average higher than those in the M1 phase, the origin and impact of which will be discussed later.

To confirm the actuation capability of the stoichiometry-tuned M2-phase NWs and quantitatively compare with the M1 phase, a prototype micro-actuator driven by individual NWs is designed and the output force across the MIT is measured in real time in the TEM (schematically demonstrated in Figs. 4(a) and 4(b)). The individual VO_2 NW is transferred and bonded to a Si-based MEMS electrical-contact-resistance push-to-pull (ePTP) device (Hysitron, Inc) [5, 34] in the dual beam focused ion beam system (FIB). The details are displayed in Fig. S7 in the ESM, as well as in our previous work [5, 35]. Originally, the ePTP device is designed to impose tensile force onto the individual NW bridging the sample trench by pushing the moving part of the ePTP at the semicircular end with a punch, and the electrical signals can be measured simultaneously [35]. In this study, however, the ePTP is employed for actuation capability measurement. A tungsten punch (Hysitron PicoIndentor) is carefully placed at the semicircular end of the moving part with a minimum contacting force F (~ 0.3 μN), ensuring that the NW is almost strain free before the MIT (Fig. 4(a)). The tungsten punch is connected with an accurate force transducer with sub-micro-newton precision. As the electric current passes through the VO_2 NW, the joule heating triggers the insulator-to-metal phase transition and causes the shortening of the crystal lattice along the NW (i.e., along the crystalline *c*-axis of the R phase). Thereby the NW tends to shrink and pushes the moving part of the ePTP. However, the punch is kept at its position under the displacement-controlled mode, which impedes the movement of the moving part and stretches the NW, keeping the NW at its original length (Fig. 4(b)). The recorded F is identical to the stretching force on the NW F_{NW}, which represents the force generated by the MIT. Thus, the corresponding stress $\sigma = F/s$ is defined as the actuation stress, where s is the cross-sectional area of the NW measured in FIB.

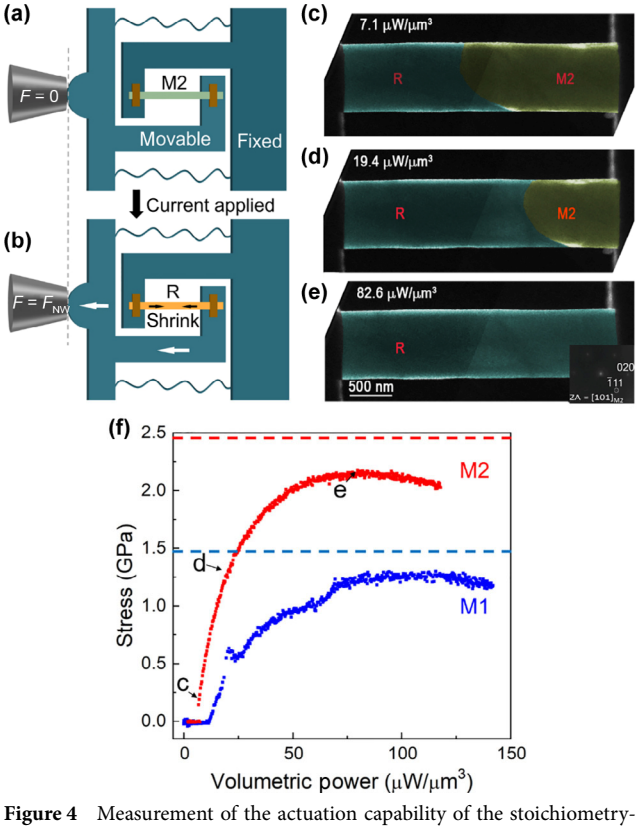

Figure 4 Measurement of the actuation capability of the stoichiometry-tuned M2-phase NWs. The schematics show the measurement of the force applied to the transducer before (a) and during (b) the joule-heating-induced MIT. (c)–(e) show the *in situ* TEM images of phase evolution of the NW. The inset in (e) shows the SADP of the NW before phase transition. The g vector $\bar{1}11$ for the dark-field images is indicated by the circle. (f) Output stress of the M1 phase (blue) and the M2 phase (red).

The stress evolution of a 17.0 μm long M2-phase NW with the cross-sectional area of 0.043 μm^2 during the joule-heating-induced MIT is investigated by simultaneously recording the force. The structure evolution is monitored by an *in situ* movie of the dark field TEM images (the g vector is $\bar{1}11$ of the M2 phase, see Movie ESM 1 in the ESM). The volumetric electric power density is defined as $P = IU/V$ to quantitatively compare the power needed to generate the actuation, where I, U, and V are the applied current, the corresponding voltage, and the volume of the NW between the two Pt patches, respectively. Three typical TEM dark field images from Movie ESM 1 in the ESM are displayed in Figs. 4(c)–4(e). At the initial stage when the joule heating generated by the electric current/power is not high enough to elevate the NW temperature above the phase transition temperature (T_{MIT}), the entire NW stays in the M2 phase, and thus uniform contrast is observed and no output strain is detected. As the temperature is further elevated by higher electric current, a sudden contrast change is observed on the left side of the view with a curvy phase boundary while the right side remains as it was. This phenomenon indicates the appearance of the R phase and incomplete MIT. The respond time is within hundreds of milliseconds (More details are shown in Fig. S8 in the ESM). From Fig. 4(f), the onset of the MIT observed in Fig. 4(c) occurs at the electric power of 7.1 μW/μm^3 with an abrupt σ jump to 0.14 GPa. As the joule heating power keeps ramping up, the NW temperature is elevated progressively. Simultaneously, heat dissipation is promoted due to the increased temperature gradient between the NW and the substrate. An equilibrium state for the M2/R phase fraction and distribution, as well as the strain and stress of the NW is achieved once the joule heating is balanced by the heat dissipation. In this process, no new nucleation sites (Fig. S9 in the ESM) or abrupt strain jump are observed. Instead, the R phase domain expands unidirectionally along the NW, and the M2–R phase boundary moves smoothly towards the M2 phase, as shown in Fig. 4(d). The output stress increases continuously as more and more segments of the NW convert into the R phase. The peak stress of 2.11 GPa is obtained at 82.6 μW/μm^3 when the M2–R phase transition is fully accomplished, evidenced by the uniform contrast in Fig. 4(e). Afterwards, the strain drops gradually at higher electric power.

The dynamic response of the actuator is studied by employing a 17.9 μm long M2-phase NW with the cross-sectional area of 0.043 μm^2. The experimental setup is also ePTP based, similar to the one shown in Fig. 4(a). A square-wave voltage is applied to tune the temperature of the NW, which consequently modulates the phase distribution and drives the motion of the ePTP device. Figure 5(a) shows the motion of the ePTP driven by the square-wave voltage alternating between 0.8 and 0.6 V at the frequency of 40 Hz in the TEM. The edge of the moving part of the ePTP is clear and sharp before the voltage is applied (left panel). When the 40 Hz square-wave voltage is applied, the oscillation of the moving part makes the edge blurry (right panel) due to the low movie frame capture frequency (10 frames/s) compared to the oscillation frequency. The oscillation of the ePTP can be interpreted by the joule-heating-controlled MIT of the M2-phase NW. When the high voltage is applied, the

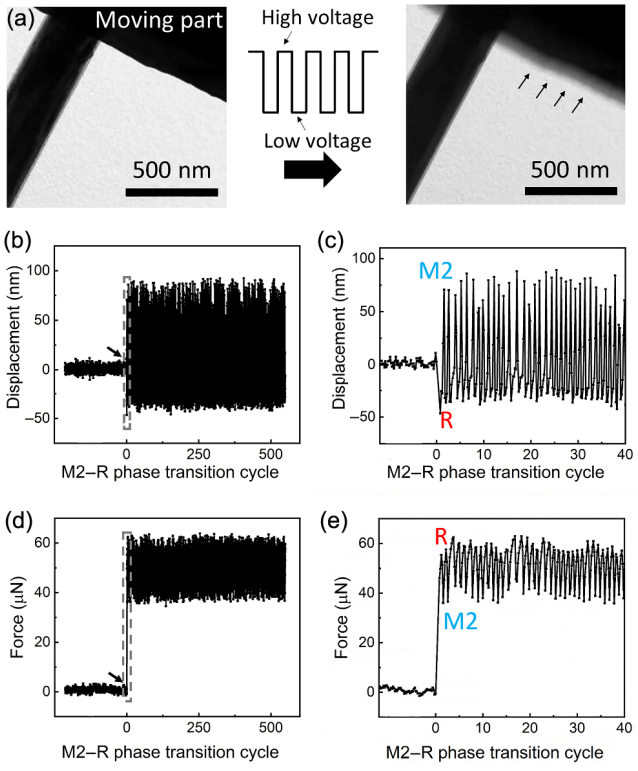

Figure 5 Actuation behavior of the M2-phase NW upon applying square-wave voltage. (a) TEM images before (left) and during (right) the square-wave voltage is applied. (b) and (d) Displacement and force of the M2-phase NW. The input of the square-wave voltage is indicated by the arrow. (c) and (e) Detailed information about the dashed rectangle part in (b) and (d), respectively.

M2-phase VO_2 NW is heated by joule heating and transforms into the R phase. The crystal lattice shrinkage along the NW drives the backward movement of the punch, indicated by the force jump and displacement drop in Figs. 5(b) and 5(d) (the force contribution from the ePTP has already been extracted). When the low voltage is applied, the NW transforms back to the M2 phase, correspondingly the force drops and the displacement increases (more details are shown in Fig. S10 in the ESM). The oscillation amplitude of the moving part of ePTP stays almost the same for the over 500 M2–R phase transition cycles. The NW remains in the M2 phase as indicated by the SADP after the cycles (Fig. S11 in the ESM). These results indicate the MIT in the M2-phase NW is fully reversible, and the M2-phase NW is stable and robust during the phase transition cycles.

Similar to previous report, the growth of NWs follows the vapor–solid mechanism [36]. The VO_2 (T_m = 1,767 °C) powder first evaporates and decomposes into low-melting-point vanadia vapor (e.g., V_2O_5 T_m = 690 °C, and V_6O_{13} T_m = 708 °C) [37], where the high-valence V^{5+} is introduced into the system. The vanadia precursors then form super-cooled liquid V_2O_5 nano-droplets, which act as the growth sites for VO_2 crystal [38]. Elevating the temperature increases the theoretical saturation pressure and actual partial pressure of the vanadia vapor. Decreasing the gas flow slows down the gas flow rate and thus increases the partial pressure of the vanadia vapor. With the elevated partial pressure of vanadia vapor, the precursors with high-valence V are supposed to deposit more rapidly on the substrate under the non-equilibrium state, which may enter and stay in the NW before fully decomposition and introduce oxygen off-stoichiometry (most likely oxygen interstitials from theoretical calculations [39]) into the NWs, as supported by the XPS results. Such rapid-growth-induced point defects have also been reported in ZnO [35, 40], quartz [41], and other semiconductors [42, 43]. The slight oxygen excess can lead to the stabilization of the M2 phase. As proposed by Pouget et al., the V^{5+} cations may rise in the neighborhood of the Cr cations for charge compensation in Cr-doped VO_2, and their ordering on one of the sublattices can stabilize the M2 phase [21]. Here in our work, the increase of V^{5+}/V^{4+} ratio is supposed to play a similar role which has shifted the phase stability between the M1 and M2 phases at ambient conditions. It is noticed that the growth of M2-phase NW has rarely been reported using the similar synthesis method in previous reports. This may be related to the differences in the vapor density and the deposition temperature due to the specific experimental setup. The power source is usually placed in open-top boat in previous work, whereas a 15 mm tube is employed in our work, thus high-density vanadia vapor is confined inside the small tube. The substrate is placed right above the source rather than being placed downstream, thus the deposition temperature is elevated to be near the evaporating temperature.

To compare the actuation ability of M2- and M1-phase NWs, an M1-phase NW with 16 μm in length and 0.075 μm^2 in cross-sectional area is tested with the same experimental setup as shown in Figs. 4(a) and 4(b), and the stress-volumetric power curve is also plotted in Fig. 4(f). Theoretically, the phase transition strain for the M2- and M1-phase NWs are 1.7% and 1%, respectively [9]. According to the Hooke's law, $\sigma = E \cdot \varepsilon$, the theoretical phase transition stress is 2.38 and 1.40 GPa, respectively, taking the elastic modulus E of all the M1, M2, and R phases as 140 GPa [5, 6, 16]. In our experiments, the joule heating induced MIT in the M2 and M1 NWs shown in Fig. 4(f) is repeated for several times, and the averaged maximum transition stress for the M2 and M1 phases is listed in Table 1. The measured values of the maximum stress are 2.09 and 1.25 GPa for the M2 and M1 phases, respectively. These values are higher than the stresses reported in VO_2-film based bimorph actuators (0.5 to 1 GPa) [44, 45]. The strain change is calculated to be 1.5% for the M2-phase NW. This value is not only by far higher than the ~ 0.3% strain change in bimorph actuators [44–46], but also higher than the value in M1-phase single-crystalline actuator (~ 1%) [16] and the M1-phase NW (0.9%) measured in our work. The volumetric work density representing the maximum mechanical work output per unit volume is calculated by $\frac{1}{2}\sigma^2/E$. The theoretical volumetric work density for the M2 phase can be calculated to be 20.2 J/cm^3. The measured value in the M2-phase NW is 15.9 J/cm^3, which is higher than the reported value for bimorph actuators (~ 0.8 J/cm^3) [4, 44, 45] and the theoretical value for the M1 phase (~ 7 J/cm^3) [4, 16].

Our measured values are reasonably consistent with the theoretical expectations. The discrepancy may arise from three

Table 1 Actuation comparison of micro-actuators driven by M2- and M1- NWs

Starting phase	Phase transition strain (%)		Phase transition stress (GPa)		Volumetric work density (J/cm^3)	Power density to trigger MIT ($\mu W/\mu m^3$)	Power density to obtain peak stress ($\mu W/\mu m^3$)
	Theoretical	Measured	Theoretical	Measured			
M2	1.70	1.50	2.38	2.09 ± 0.03	15.9	7.2 ± 1.8	79.0 ± 3.2
M1	1.00	0.90	1.4	1.25 ± 0.04	5.8	12.5 ± 3.4	96.2 ± 6.1

reasons. Firstly, the lattice change in the nonstoichiometric M2-phase NWs may be slightly different from the pristine ones. Secondly, the thermal expansion of the NWs at elevated temperature cancels out a portion of the tensile stress (the temperature distribution is further discussed, see Fig. S12 in the ESM). Finally, there are possible errors in the experiment such as misalignment of the NWs with respect to the trench. It is noticed that as listed in Table 1, less volumetric power is required to trigger the M2–R transition than the M1–R transition. In pure VO_2, T_{MIT} for the M2 phase is higher than that of the M1 phase. However, when the M2 phase is stabilized to room temperature by tuning the stoichiometry, the bias of the T_{MIT} for the M2 phase from the T_{MIT} for the M1 phase is insignificant compared to the stress effect (Fig. S13 in the ESM). In our samples, the M2-phase NWs contain more oxygen interstitials (as discussed in Fig. 3(e)) with respect to the M1 phase. These oxygen interstitials in the M2 phase can scatter the phonons and consequently decrease the thermal conductivity of the M2 phase. Hence the thermal conduction to the substrate can be less sufficient in the M2-phase NW than that in the M1-phase NW, which costs less MIT triggering power. Moreover, measurement error can be introduced by the microscopic dissipation conditions (such as the length of the NW and the contact area of the NW with the substrate).

3 Conclusions

In conclusion, we have successfully synthesized free-standing single-crystalline M2-phase VO_2 NWs via a simple thermal evaporation method. The high-yield M2-phase NWs are achieved at higher temperature and lower carrier gas flux rate. XPS study confirms that under such condition the oxidation state of the V cations is higher than that with M1-phase, proving that the phase of VO_2 NWs is modulated using the chemical method, which is non-martensitic and easy-to-access via synthetic condition control. Higher oxygen excess favors the stability of the M2 phase. *In situ* electrical-force coupled testing approach is applied to investigate quantitatively the actuation stress of the micro-actuator driven by VO_2 NWs, which confirms that the M2 phase outputs 65% higher stress than the M1 phase. Our study has demonstrated and realized, from materials synthesis to actuation stress measurement, the individual M2-phase VO_2-NW-based micro-actuators exhibit significantly superior actuation capability.

4 Methods

Controllable synthesis of VO_2 NWs: Commercial VO_2 powder (purity 99%, Alfa Aesar) is placed in a carrying quartz tube in the center of a horizontal tube furnace. Unpolished (rough) silicon substrates are placed about 5 mm above the source for higher vapor density and deposition temperature. The furnace tube is first evacuated to the base pressure of ~ 10^{-2} Torr and purged with Ar for several times. The temperature is then ramped up at the rate of 15 °C/min and kept at the target temperature for ~ 5 h. The pressure is maintained at approximately 10 Torr during the whole process. A wide range of growth temperature (from 700 to 1,000 °C) and the Ar flow rate (50 to 400 sccm) are tuned to optimize the growth conditions for the M2 phase. The morphology, the length and diameter distribution, the crystal quality, and the as-grown phase are characterized with the SEM (Hitachi S6600), TEM (JEOL 2100F, 200 kV), and confocal micro-Raman spectra.

Raman characterization: The as-grown phase of the NWs is characterized with micro-focused HeNe Laser (λ = 633 nm) in Horiba Jobin-Yvon LabRam HR800. The laser spot size is around 1 μm. The NWs obtained on the rough silicon are free-standing, ensuring the external strain effect is avoided in the Raman measurement. The acquisition time is ~ 5 min to achieve good signal-to-noise ratio in the Raman spectra for individual NWs. For Raman mapping, a 50 × objective lens with numerical aperture (NA) = 0.95 is used. A piezo stage is used to move the sample with the step of about 1 μm, taking a Raman spectrum at each point with an integration time of 10 s. The spectra are analyzed, and the Raman mappings of the dominant peak (~ 650 and 610 cm^{-1} for the M2 and M1 phases, respectively) intensity are conducted.

XPS characterizations: XPS studies are carried out on fresh sample surfaces in a Kratos Axis Ultra DLD spectrometer equipped with a monochromatic Al Kα X-ray source ($h\nu$ = 1,486.6 eV) operating at 150 W, a multichannel plate, and delay line detector under a vacuum of 1×10^{-9} mbar. The survey and high-resolution spectra are collected at fixed analyzer pass energies of 160 and 20 eV, respectively. Binding energies are referenced to the C 1s peak (set at 284.4 eV) of the sp^2 hybridized (C=C) carbon from the sample.

Individual NWs transfer to the ePTP device: The individual VO_2 on the ePTP is prepared in the dual-beam FIB (FEI Helios 600). The as-grown free-standing VO_2 NWs are first transferred to the copper grid by gently rubbing the grid against the substrate. The difficulty in transferring the NW can be greatly reduced as most NWs are separated from each other and lying on the grid without tilting. By using the Kleindiek micromanipulator, the individual NW is transferred to the specimen trench, well aligned with the motion direction of the tungsten punch to ensure precise force measurements. Both ends of the NW are bonded to the Au electrodes by electron beam induced Pt deposition. The Ga ion is only exposed to the very end of the NW to cut the NW off the probe of the micromanipulator in the whole process, so the Ga ion irradiation as well as the Pt pollution are minimized.

In situ characterization of the joule heating induced MIT in TEM: The uniaxial loading condition is ensured by the careful alignment of the NW and the special design of the dimensions and anisotropy stiffness of the springs in the ePTP device. For Fig. 4, the electric current is applied to the sample in a current control mode at a current ramping rate in the range of 1 to 10 μA/s. It is still under debate whether the MIT in VO_2 is triggered by the electric field or the joule heating. Both the electric field breakdown model and joule heating model are established [47]. In the electric field breakdown model, the MIT occurs when the electron density is increased to the critical value 3×10^{18} cm^{-3} by electric field. The value of theoretical electric field E_c required to generate such high electron density is 50 V/μm [48]. In all of experiments in our work, the applied electric field is less than 0.075 V/μm, which is 3 orders of magnitudes lower than the critical value. So the electric field breakdown model can be safely ignored. The joule heating model is applied, in which the MIT occurs when the temperature of the sample is elevated above T_{MIT} by joule heating [49, 50]. The specimen trench stays in the field of view of the TEM during the whole MIT process. And the dark-field video of the sample, as well as the mechanical response of the NW are recorded in real time. This *in situ* testing setup can also potentially be applied to the investigation of the microstructure and mechanical behaviors of other phase-transition materials.

Acknowledgements

This work was supported by the National Natural Science Foundation of China (Nos. 52031011, 91860109, 51927801, and

51621063), the National Key Research and Development Program of China (Nos. 2017YFB0702001 and 2016YFB0700404), 111 Project 2.0 of China (No. BP2018008), and funding from the Science and Technology Departments of Shaanxi and Xi'an, China (Nos. 2016KTZDGY-04-03, 2016KTZDGY-04-04, and 201805064ZD15CG48). The authors appreciate the helpful discussions and suggestions from Prof. Evan Ma from John Hopkins University (JHU). Y. Q. Z. acknowledges King Abdullah University of Science & Technology (KAUST) to support his six-months research and study at KAUST as an exchange student. We also appreciate the support from the International Joint Laboratory for Micro/ Nano Manufacturing and Measurement Technologies, and the Collaborative Innovation Center of High-End Manufacturing Equipment at Xi'an Jiaotong University, China. J. L. acknowledges support by National Science Foundation (No. CMMI-1922206). Authors declare no competing interests.

Electronic Supplementary Material: Supplementary material (characterization of the VO_2 NWs, setup for phase transition tests, the Raman spectra of the NW, Raman images of individual VO_2 NWs, strain–stress curves of M2- and M1-phase NWs in uniaxial tension test, temperature distribution of the NWs, the nucleation sites of the R phase, response speed, and *in situ* movie for the phase transition of the M2 phase NW) is available in the online version of this article at https://doi.org/10.1007/s12274-021-3355-6.

References

[1] Mirfakhrai, T.; Madden, J. D. W.; Baughman, R. H. Polymer artificial muscles. *Mater. Today* **2007**, *10*, 30–38.

[2] Vaia, R.; Baur, J. Adaptive composites. *Science* **2008**, *319*, 420–421.

[3] Smela, E. Conjugated polymer actuators for biomedical applications. *Adv. Mater.* **2003**, *15*, 481–494.

[4] Liu, K.; Cheng, C.; Cheng, Z. T.; Wang, K.; Ramesh, R.; Wu, J. Q. Giant-amplitude, high-work density microactuators with phase transition activated nanolayer bimorphs. *Nano Lett.* **2012**, *12*, 6302–6308.

[5] Guo, H.; Chen, K.; Oh, Y.; Wang, K.; Dejoie, C.; Syed Asif, S. A.; Warren, O. L.; Shan, Z. W.; Wu, J.; Minor, A. M. Mechanics and dynamics of the strain-induced M_1-M_2 structural phase transition in individual VO_2 nanowires. *Nano Lett.* **2011**, *11*, 3207–3213.

[6] Sepúlveda, N.; Rúa, A.; Cabrera, R.; Fernández, F. Young's modulus of VO_2 thin films as a function of temperature including insulator-to-metal transition regime. *Appl. Phys. Lett.* **2008**, *92*, 191913.

[7] Fan, W.; Huang, S.; Cao, J.; Ertekin, E.; Barrett, C.; Khanal, D. R.; Grossman, J. C.; Wu, J. Superelastic metal-insulator phase transition in single-crystal VO_2 nanobeams. *Phys. Rev. B* **2009**, *80*, 241105(R).

[8] Cao, J.; Gu, Y.; Fan, W.; Chen, L. Q.; Ogletree, D. F.; Chen, K.; Tamura, N.; Kunz, M.; Barrett, C.; Seidel, J. et al. Extended mapping and exploration of the vanadium dioxide stress-temperature phase diagram. *Nano Lett.* **2010**, *10*, 2667–2673.

[9] Park, J. H.; Coy, J. M.; Kasirga, T. S.; Huang, C. M.; Fei, Z. Y.; Hunter, S.; Cobden, D. H. Measurement of a solid-state triple point at the metal-insulator transition in VO_2. *Nature* **2013**, *500*, 431–434.

[10] Rúa, A.; Fernández, F. E.; Hines, M. A.; Sepúlveda, N. Study of the resonant frequencies of silicon microcantilevers coated with vanadium dioxide films during the insulator-to-metal transition. *J. Appl. Phys.* **2010**, *107*, 053528.

[11] Rúa, A.; Cabrera, R.; Coy, H.; Merced, E.; Sepúlveda, N.; Fernández, F. E. Phase transition behavior in microcantilevers coated with M_1-phase VO_2 and M_2-phase VO_2:Cr thin films. *J. Appl. Phys.* **2012**, *111*, 104502.

[12] Liu, K.; Cheng, C.; Suh, J.; Tang-Kong, R.; Fu, D. Y.; Lee, S.; Zhou, J.; Chua, L. O.; Wu, J. Q. Powerful, multifunctional torsional micromuscles activated by phase transition. *Adv. Mater.* **2014**, *26*, 1746–1750.

[13] Tian, Z.; Xu, B. R.; Hsu, B.; Stan, L.; Yang, Z.; Mei, Y. F. Reconfigurable vanadium dioxide nanomembranes and microtubes with controllable phase transition temperatures. *Nano Lett.* **2018**, *18*, 3017–3023.

[14] Cao, J. B.; Fan, W.; Zhou, Q.; Sheu, E.; Liu, A. W.; Barrett, C.; Wu, J. Colossal thermal-mechanical actuation via phase transition in single-crystal VO_2 microcantilevers. *J. Appl. Phys.* **2010**, *108*, 083538.

[15] Wang, K.; Cheng, C.; Cardona, E.; Guan, J. Y.; Liu, K.; Wu, J. Q. Performance limits of microactuation with vanadium dioxide as a solid engine. *ACS Nano* **2013**, *7*, 2266–2272.

[16] Shi, R.; Cai, X. B.; Wang, W. J.; Wang, J. W.; Kong, D. J.; Cai, N. D.; Chen, P. C.; He, P. G.; Wu, Z. F.; Amini, A. et al. Single-crystalline vanadium dioxide actuators. *Adv. Funct. Mater.* **2019**, *29*, 1900527.

[17] Pouget, J. P.; Launois, H.; D'Haenens, J. P.; Merenda, P.; Rice, T. M. Electron localization induced by uniaxial stress in pure VO_2. *Phys. Rev. Lett.* **1975**, *35*, 873–875.

[18] Brückner, W.; Gerlach, U.; Thuss, B. Phase diagram of $V_{1-x}Al_xO_2$. *Phys. Stat. Sol. (a)* **1977**, *40*, K131–K134.

[19] Strelcov, E.; Tselev, A.; Ivanov, I.; Budai, J. D.; Zhang, J.; Tischler, J. Z.; Kravchenko, I.; Kalinin, S. V.; Kolmakov, A. Doping-based stabilization of the M_2 phase in free-standing VO_2 nanostructures at room temperature. *Nano Lett.* **2012**, *12*, 6198–6205.

[20] Lee, S.; Cheng, C.; Guo, H.; Hippalgaonkar, K.; Wang, K.; Suh, J.; Liu, K.; Wu, J. Q. Axially engineered metal-insulator phase transition by graded doping VO_2 nanowires. *J. Am. Chem. Soc.* **2013**, *135*, 4850–4855.

[21] Pouget, J. P.; Launois, H.; Rice, T. M.; Dernier, P.; Gossard, A.; Villeneuve, G.; Hagenmuller, P. Dimerization of a linear heisenberg chain in the insulating phases of $V_{1-x}Cr_xO_2$. *Phys. Rev. B* **1974**, *10*, 1801–1815.

[22] Wang, Y. P.; Sun, X.; Chen, Z. Z.; Cai, Z. H.; Zhou, H.; Lu, T. M.; Shi, J. Defect-engineered epitaxial $VO_{2\pm\delta}$ in strain engineering of heterogeneous soft crystals. *Sci. Adv.* **2018**, *4*, eaar3679.

[23] Strelcov, E.; Davydov, A. V.; Lanke, U.; Watts, C.; Kolmakov, A. *In situ* monitoring of the growth, intermediate phase transformations and templating of single crystal VO_2 nanowires and nanoplatelets. *ACS Nano* **2011**, *5*, 3373–3384.

[24] Zhang, S. X.; Kim, I. S.; Lauhon, L. J. Stoichiometry engineering of monoclinic to rutile phase transition in suspended single crystalline vanadium dioxide nanobeams. *Nano Lett.* **2011**, *11*, 1443–1447.

[25] Zhou, X. C.; Andoy, N. M.; Liu, G. K.; Choudhary, E.; Han, K. S.; Shen, H.; Chen, P. Quantitative super-resolution imaging uncovers reactivity patterns on single nanocatalysts. *Nat. Nanotechnol.* **2012**, *7*, 237–241.

[26] Winkler, J.; Neubert, M. 28 - Automation of crystal growth from melt. In *Handbook of Crystal Growth*; 2nd ed. Rudolph, P., Ed.; Elsevier: Boston, 2015; pp 1143–1184.

[27] Guiton, B. S.; Gu, Q.; Prieto, A. L.; Gudiksen, M. S.; Park, H. Single-crystalline vanadium dioxide nanowires with rectangular cross sections. *J. Am. Chem. Soc.* **2005**, *127*, 498–499.

[28] McWhan, D. B.; Marezio, M.; Remeika, J. P.; Dernier, P. D. X-ray diffraction study of metallic VO_2. *Phys. Rev. B* **1974**, *10*, 490–495.

[29] Jones, A. C.; Berweger, S.; Wei, J.; Cobden, D.; Raschke, M. B. Nano-optical investigations of the metal-insulator phase behavior of individual VO_2 microcrystals. *Nano Lett.* **2010**, *10*, 1574–1581.

[30] Atkin, J. M.; Berweger, S.; Chavez, E. K.; Raschke, M. B.; Cao, J. B.; Fan, W.; Wu, J. Q. Strain and temperature dependence of the insulating phases of VO_2 near the metal-insulator transition. *Phys. Rev. B* **2012**, *85*, 020101(R).

[31] Basu, R.; Srihari, V.; Sardar, M.; Srivastava, S. K.; Bera, S.; Dhara, S. Probing phase transition in VO_2 with the novel observation of low-frequency collective spin excitation. *Sci. Rep.* **2020**, *10*, 1977.

[32] Shvets, P.; Dikaya, O.; Maksimova, K.; Goikhman, A. A review of Raman spectroscopy of vanadium oxides. *J. Raman Spectrosc.* **2019**, *50*, 1226–1244.

[33] Silversmit, G.; Depla, D.; Poelman, H.; Marin, G. B.; De Gryse, R. Determination of the V_{2p} xps binding energies for different vanadium oxidation states (V^{5+} to V^{0+}). *J. Electron Spectros. Relat. Phenomena* **2004**, *135*, 167–175.

[34] Guo, H.; Wang, K.; Deng, Y.; Oh, Y.; Syed Asif, S. A.; Warren, O. L.; Shan, Z. W.; Wu, J.; Minor, A. M. Nanomechanical actuation from phase transitions in individual VO_2 micro-beams. *Appl. Phys. Lett.* **2013**, *102*, 231909.

[35] Wang, X. G.; Chen, K.; Zhang, Y. Q.; Wan, J. C.; Warren, O. L.; Oh, J.; Li, J.; Ma, E.; Shan, Z. W. Growth conditions control the elastic and electrical properties of ZnO nanowires. *Nano Lett.* **2015**, *15*, 7886–7892.

[36] Cheng, C.; Liu, K.; Xiang, B.; Suh, J.; Wu, J. Q. Ultra-long, free-standing, single-crystalline vanadium dioxide micro/nanowires grown by simple thermal evaporation. *Appl. Phys. Lett.* **2012**, *100*, 103111.

[37] Yang, Z.; Ko, C.; Ramanathan, S. Oxide electronics utilizing ultrafast metal-insulator transitions. *Annu. Rev. Mater. Res.* **2011**, *41*, 337–367.

[38] Kim, M. H.; Lee, B.; Lee, S.; Larson, C.; Baik, J. M.; Yavuz, C. T.; Seifert, S.; Vajda, S.; Winans, R. E.; Moskovits, M. et al. Growth of metal oxide nanowires from supercooled liquid nanodroplets. *Nano Lett.* **2009**, *9*, 4138–4146.

[39] Cui, Y. Y.; Liu, B.; Chen, L. L.; Luo, H. J.; Gao, Y. F. Formation energies of intrinsic point defects in monoclinic VO_2 studied by first-principles calculations. *AIP Adv.* **2016**, *6*, 105301.

[40] Kortunova, E. V.; Nikolaeva, N. G.; Chvanski, P. P.; Maltsev, V. V.; Volkova, E. A.; Koporulina, E. V.; Leonyuk, N. I.; Kuech, T. F. Hydrothermal synthesis of improved ZnO crystals for epitaxial growth of gan thin films. *J. Mater. Sci.* **2008**, *43*, 2336–2341.

[41] Martin, J. J.; Armington, A. F. Effect of growth rate on quartz defects. *J. Cryst. Growth* **1983**, *62*, 203–206.

[42] Tanahashi, K.; Kikuchi, M.; Higashino, T.; Inoue, N.; Mizokawa, Y. Concentration of point defects changed by thermal stress in growing CZ silicon crystal: Effect of the growth rate. *J. Cryst. Growth* **2000**, *210*, 45–48.

[43] Hurle, D. T. J.; Rudolph, P. A brief history of defect formation, segregation, faceting, and twinning in melt-grown semiconductors. *J. Cryst. Growth* **2004**, *264*, 550–564.

[44] Rúa, A.; Fernández, F. E.; Sepúlveda, N. Bending in VO_2-coated microcantilevers suitable for thermally activated actuators. *J. Appl. Phys.* **2010**, *107*, 074506.

[45] Merced, E.; Tan, X. B.; Sepúlveda, N. Strain energy density of VO_2-based microactuators. *Sens. Actuator. A: Phys.* **2013**, *196*, 30–37.

[46] Huang, C. Z.; Zhang, Z.; Ramanathan, S.; Weinstein, D. VO_2 phase-transition-based vertical MEMS microactuators. *IEEE Trans. Electron Dev.* **2019**, *66*, 4380–4386.

[47] Yoon, J.; Lee, G.; Park, C.; Mun, B. S.; Ju, H. Investigation of length-dependent characteristics of the voltage-induced metal insulator transition in VO_2 film devices. *Appl. Phys. Lett.* **2014**, *105*, 083503.

[48] Hormoz, S.; Ramanathan, S. Limits on vanadium oxide mott metal–insulator transition field-effect transistors. *Solid-State Electron.* **2010**, *54*, 654–659.

[49] Simon Mun, B.; Yoon, J.; Mo, S. K.; Chen, K.; Tamura, N.; Dejoie, C.; Kunz, M.; Liu, Z.; Park, C.; Moon, K. et al. Role of joule heating effect and bulk-surface phases in voltage-driven metal-insulator transition in VO_2 crystal. *Appl. Phys. Lett.* **2013**, *103*, 061902.

[50] Zimmers, A.; Aigouy, L.; Mortier, M.; Sharoni, A.; Wang, S. M.; West, K. G.; Ramirez, J. G.; Schuller, I. K. Role of thermal heating on the voltage induced insulator-metal transition in VO_2. *Phys. Rev. Lett.* **2013**, *110*, 056601.

Electronic Supplementary Material

Achieving room-temperature M_2-phase VO_2 nanowires for superior thermal actuation

Yong-Qiang Zhang[1,§], Kai Chen[1,§], Hao Shen[1], Yue-Cun Wang[1], Mohamed Nejib Hedhili[2], Xixiang Zhang[2], Ju Li[3] (✉), and Zhi-Wei Shan[1] (✉)

[1] *Center for Advancing Materials Performance from the Nanoscale, State Key Laboratory for Mechanical Behavior of Materials, Xi'an Jiaotong University, Xi'an 710049, China*

[2] *Physical Science and Engineering Division, King Abdullah University of Science and Technology (KAUST), Thuwal 23955-6900, Saudi Arabia*

[3] *Departments of Nuclear Science and Engineering and Materials Science and Engineering, Massachusetts Institute of Technology, Cambridge, MA 02139, USA*

[§] *Yong-Qiang Zhang and Kai Chen contributed equally to this work.*

Supporting information to https://doi.org/10.1007/s12274-021-3355-6

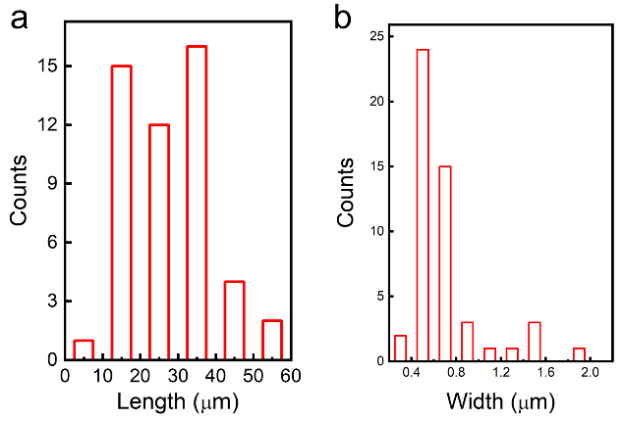

Figure S1 (a) Length and (b) width distribution of the NWs grown at 1000 °C with the Ar flow of 50 sccm displayed in Figure 2b.

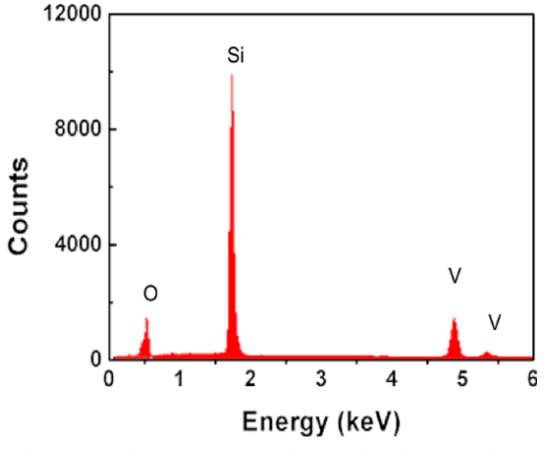

Figure S2 The EDS spectra of individual M2-phase NWs shows no impurity elements besides V, O. The Si signal is from the substrate.

Address correspondence to Zhi-Wei Shan, zwshan@mail.xjtu.edu.cn; Ju Li, liju@mit.edu

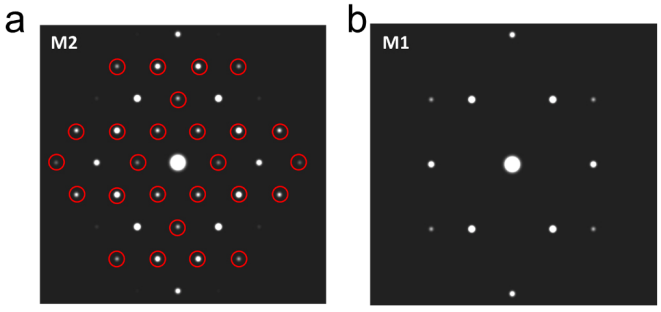

Figure S3 The simulated selected area diffraction patterns (SADP) of (a) M2 phase and (b) M1 phase in the zone axis of $[001]_{M2}$ (or equivalently $[102]_{M1}$). The zone axis of the simulated SADP is the same as in Figure 2c. Although the SADP of the M2 and M1 phase are quite similar due to their similar crystal structure and parameters, the lower symmetry of the M2 phase leads to extra diffraction spots in the presented viewing directions. The M2 phase can be distinguished from the M1 phase by the extra diffraction spots (as indicated by the circles) which do not show up in the SADP of the M1 phase.

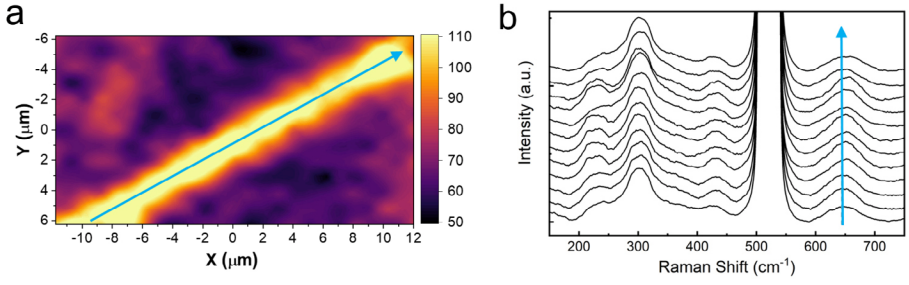

Figure S4 (a) The Raman image of the M2-phase NW shown in Figure 3b. (b) A series of twelve Raman spectra is taken along the NW as indicated by the blue line. The dominated peak appears at about 650 cm^{-1} in all spectra with almost uniform Raman intensity, indicating the whole NW is in the M2 phase.

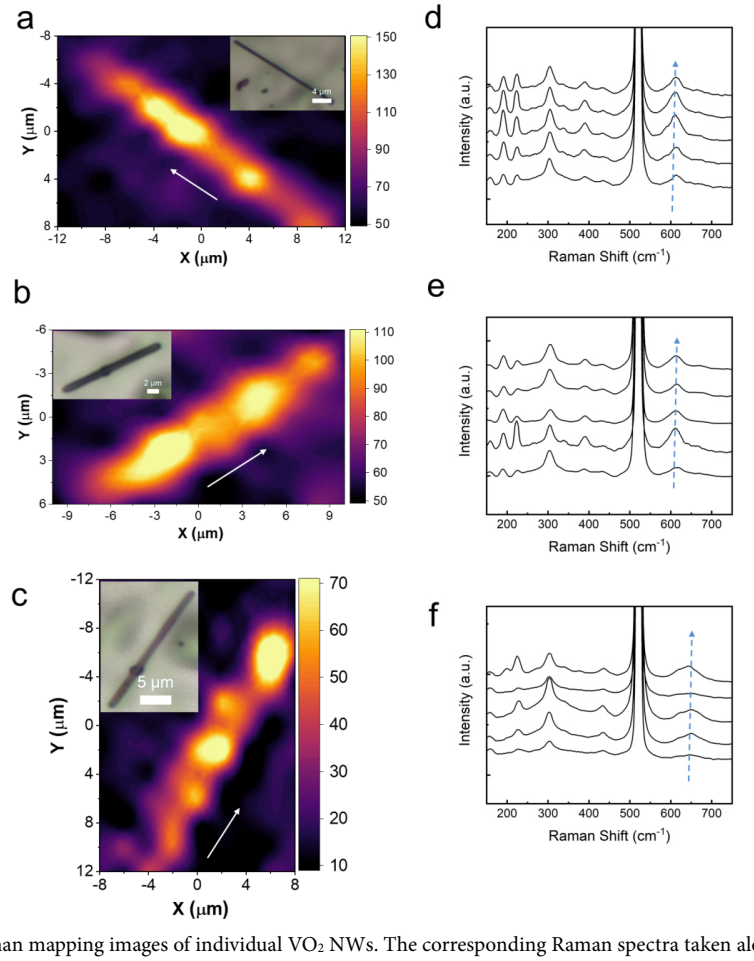

Figure S5 (a)-(c) show the Raman mapping images of individual VO_2 NWs. The corresponding Raman spectra taken along the NW are displayed in (d), (e) and (f), respectively. The NWs in (a) and (b) are in the M1 phase, and the NW in (c) is in the M2 phase. These images are obtained by extracting the peak intensity at 610 cm^{-1}, 612 cm^{-1} and 650 cm^{-1}, respectively. These results indicates both the M1-and M2-phase NWs are occupied by a single phase. The non-uniform contrast of the NW is resulted from the spatial resolution limitation on small samples, i.e. the diameter of the NWs is much smaller than the beam size as well as the step size of the stage. Consequently, the non-uniform contrast is just the reflection of the different proportion of the signal from the NWs and the substrate as well as the discontinuous data collection in space.

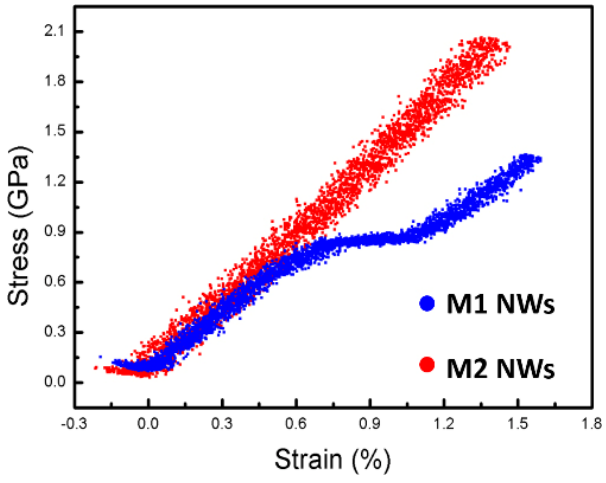

Figure S6 The tensile stress-strain curve of the M1- and M2-phase NWs, indicating the M2-phase NW does not contain any M1-phase components.

To distinguish the M1 and M2 phase, the uniaxial tensile test is to carry out by using the PTP device in our experimental setup in the TEM [1]. The strain-stress curves show dramatic difference between the M1-phase NW and M2-phase NW. The strain-stress curve of the M1 phase shows a characteristic stress plateau reflecting the M1-M2 phase transition. On contrast, the strain stress curve of the M2 phase is linear. This phenomena strongly evidence that the M2-phase NW does not contain any M1-phase components, otherwise there will also be a stress plateau, whose length depends on the fraction of the M1-phase.

Table S1 the V/O ratio and the stoichiometry of the M2- and M1-phase NWs

	M2	M1
V/O ratio	0.43	0.45
Stoichiometry	$VO_{2.29}$	$VO_{2.21}$

The stoichiometry of the NW is calculated by the valence states of the vanadium atoms [2, 3]. As the binding energy of $V2p_{3/2}$ depends on the valence of the V cations, the V/O ratio can be calculated, V/O ratio$=\frac{2}{5p(V^{5+})+4p(V^{4+})}$

Where $p(V^{4+})$ is the proportion of V^{4+} cations and $p(V^{5+})$ is the proportion of V^{5+} cations. These values have been obtained by curve fitting the $V2p_{3/2}$ as shown in Figure 3e. The stoichiometry of M2- and M1-phase NWs are $VO_{2.29}$ and $VO_{2.21}$, respectively. The M2-phase NWs shows higher oxygen excess than the M1-phase NWs.

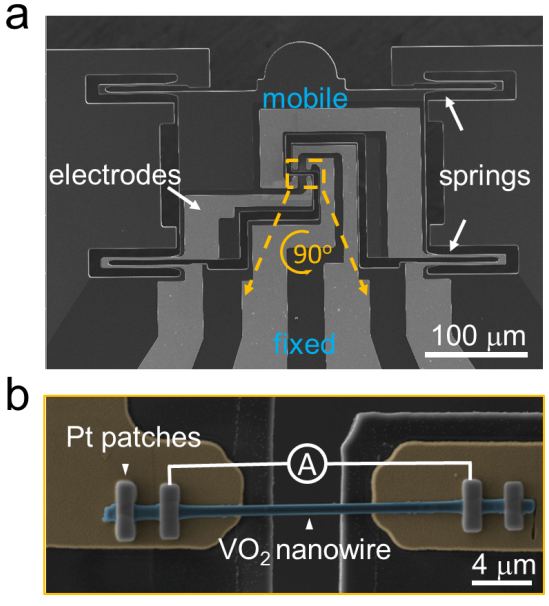

Figure S7 The SEM image of (a) the ePTP device and (b) the VO_2 NW bridging the trench.

An individual VO_2 NW is transferred to the ePTP device using the Kleindiek micromanipulator in the dual beam focused-ion beam system (FIB). The NW is then carefully aligned perpendicular to the specimen trench to ensure precise mechanical measurement, and bonded to the Au electrodes achieved by electron-beam induced Pt deposition to minimize ion irradiation damage and pollution.

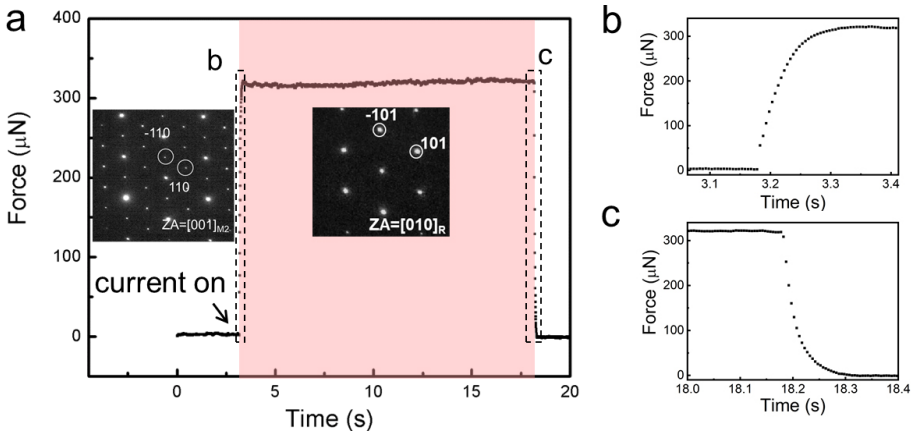

Figure S8 (a) The force-time curve showing the mechanical response of the device when the 80 μA electrical current pulse is applied. The insets are the SADP before (left) and after (right) the phase transition. The force rise/fall upon the current is turned on/off indicated by the dashed rectangle in (a) are magnified in (b) and (c).

The response time of the actuator device is tested. The experimental setup is the same as the setup in Figure 4. Electrical current of 80 μA is applied to the actuator device. The force jumped to ~310 μN when the current is applied, and the SADP change before and after the force jump shown in the inset in Figure S11 indicates the phase transition from the M2 phase to the R phase. Taking advantage of the high temporal resolution of the force transducer (200 points/s), the force evolution upon the current is turned on/off are shown in Figure S8 b and c. It can be seen that the force rise/fall accomplishes in about 0.15s and 0.13s, respectively. The working frequency with full M2-R phase transition is limited below 6 Hz.

This working frequency is much lower than the reported value (~2 kHz) in VO_2-based bimorph actuators [4]. This slow response speed may be caused by the strain-induced expansion of phase transition temperature T_{MIT}. Once the R phase is nucleated in the length-fixed NW in our experiment, the tensile strain induced by the lattice shrinkage will elevate the phase transition temperature T_{MIT}. The T_{MIT} is further elevated as more M2 phase transforms into the R phase progressively. Thus the increasing T_{MIT} during the phase transition can lead to the expansion of transition time. The working frequency can be improved by reducing the external load. Reducing the applied force to the device enables the length change of the NW. Consequently the strain effect on the T_{MIT} is weaker and the phase transition speed can be improved.

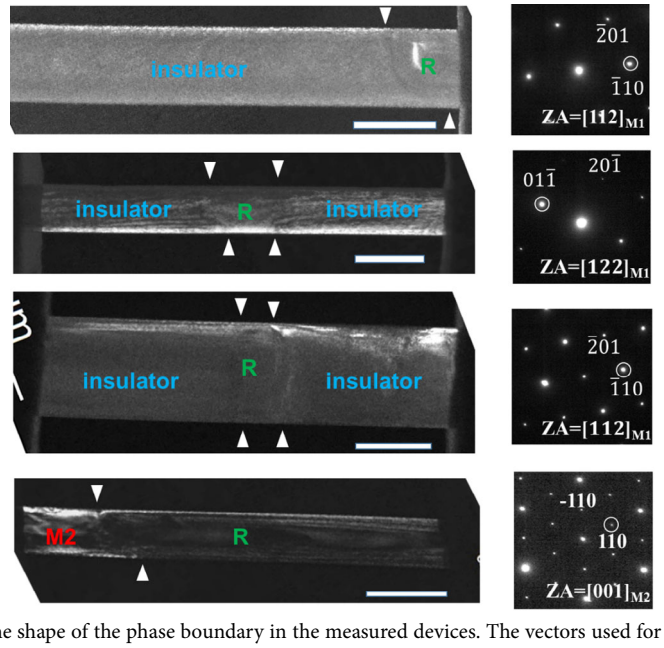

Figure S9 The nucleation site and the shape of the phase boundary in the measured devices. The vectors used for dark-field images are indicated by the circles in the corresponding SADPs on the right. The chosen g vectors exist only in the M1 and M2 phase and vanish in the R phase due to structure change. The NWs are rotated 68 degrees clockwise. The scale bars are 500 nm.

The middle of the NW is expected to be the hot part and thus the incipient position of MIT, and it has been proved that this rule works in most of the NWs tested in this work. Several examples are shown. Occasionally, the R phase nucleates at elsewhere outside the field of view in the trench, caused by the imperfect microscopic details in real devices, such as asymmetric thermal dissipation conditions on both sides of the NW, and/or the grown-in microstructural defects that serve as the nucleation sites in the NW. Moreover, the shape of the phase boundaries is sample dependent, maybe also related to the initial defect distribution in the NWs.

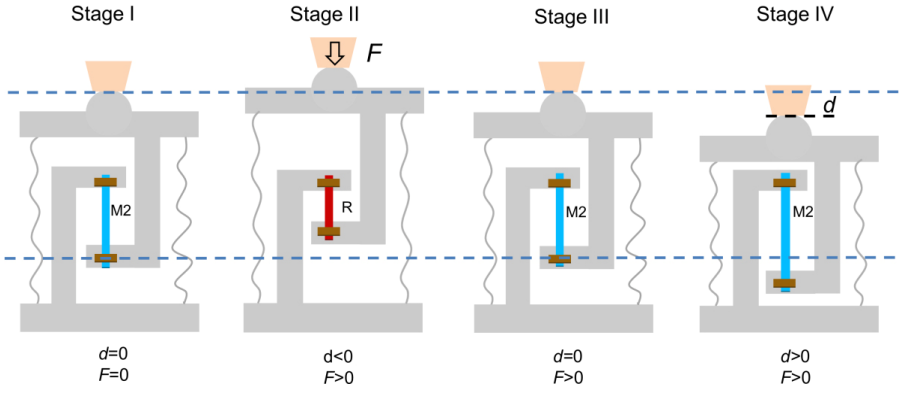

Figure S10 The schematics showing the displacement and force evolutions when the square-wave voltage is applied. The positive directions for the force and displacement is indicated in stage II and stage IV, respectively.

The dynamic process of the device when applying the square-wave voltage is illustrated. Stage I shows the experimental setup before applying the square-wave voltage. The tungsten punch equipped with a force transducer is carefully placed at the semicircular end of the moving part in the displacement control mode. In this mode, the displacement d sensitively shows the length change of the NW. The force F is applied in response to d to push the semicircular end towards its original position (where d=0 as shown in stage I). When the high voltage is applied as shown in stage II, the M2-R phase transition is induced by joule heating, the lattice shrinkage drives the backward movement of moving part along with the tungsten punch (d<0). Consequently positive F is applied in response. When the voltage is shifted to the low voltage at high frequency (40 Hz) as shown in stage III, the NW transforms back to the M2 phase as the temperature is cooled down below T_{MIT} and the NW elongates to its original length (d=0). The applied force, however, is PID controlled and is lagged behind the displacement change. The force is decreased but is not tuned to the expected value of zero in time, so there is still a positive force applied by the punch. Consequently the force continues to push the semicircle end moving forward, as shown in stage IV. Both positive d and F are observed in this stage. Before the force equilibrium (where F should be negative) is established, the high voltage is again switched on at the frequency of 40 Hz, the M2-R transition is induced again, and the device goes back to stage II. As the square-wave voltage is applied, the MIT occurs back and forth and the device goes through stage II to stage IV repeatedly.

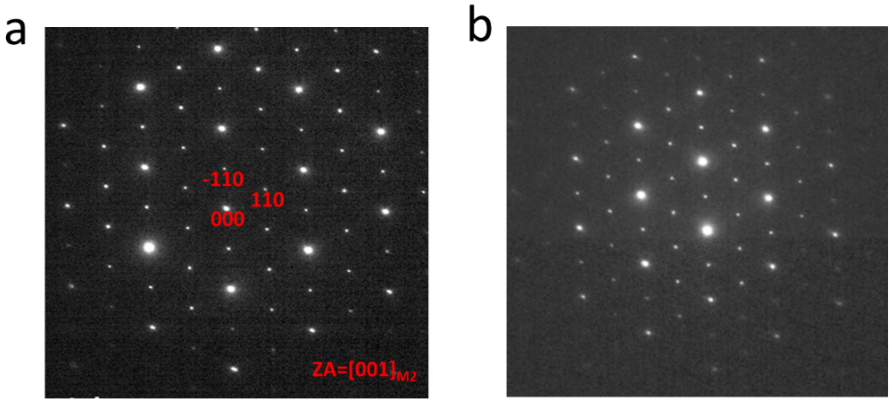

Figure S11 The SADP before (a) and (b) after the M2-R phase transition cycles shown in Figure 5. The SADP remains almost the same, indicating the crystal structure did not change after the phase transitions.

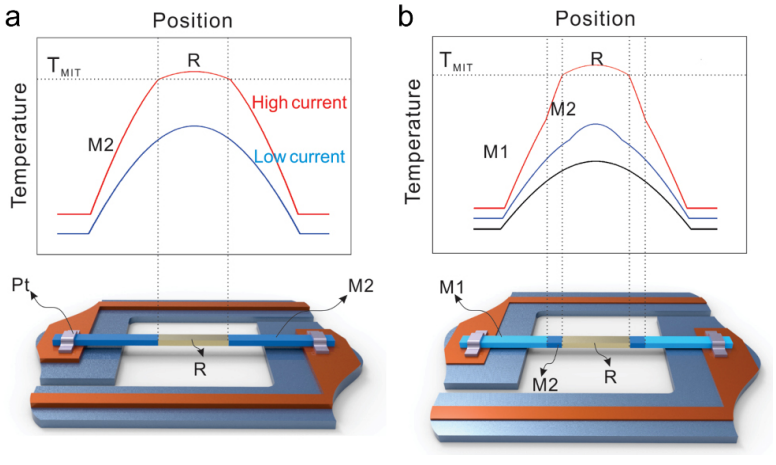

Figure S12 (a) The estimated temperature distribution in the joule heating process on the M2-phase (a) and M1-phase (b) VO_2 NW at fixed length.

It is worth noticing that the temperature becomes non-uniform along the NW once the electric current is applied, which plays a crucial role in determining the phase configuration in the VO_2 NW. The temperature distribution along the NW can be calculated based on the one-dimensional heat conduction model [5],

$$\frac{\partial^2 T}{\partial x^2} = -\frac{Q}{\kappa} = -\frac{I^2 R / L}{\kappa} \quad (1)$$

where T is the temperature at the given position on the NW, Q is the heat flow rate through the NW, κ is the thermal conductive of VO_2, I is the current applied to the NW, R is the resistance, and L is the length of the NW. The temperature of the pads near the NW are treated as uniform for simplification. As the electrical power ramps up, the NW temperature is elevated progressively, and the heat dissipation is also enhanced simultaneously due to the increased temperature difference between the NW and the substrate. An equilibrium state for the M2/R phase fraction and distribution, as well as the strain and stress of the NW is achieved as soon as the joule heating is balanced by the heat dissipation. The highest temperature appears in the middle of the trench. At low current before MIT (the blue curve), the temperature decreases parabolically from the center. When the temperature reaches T_{MIT} at high current (the red curve), the central part of the NW firstly transforms into the R phase, while the other parts remains in the M2 phase. The temperature in the R phase is much more uniform than in the M2 phase, because the electrical resistance and joule heating efficiency of the metallic R phase are orders of magnitude lower than those of the M2 phase. The phase reconfiguration in the M1 phase is more complicated, because the M2 phase is involved in the intermediate state under tensile strain as shown in Figure S12 b. This may explain why a kink shows up in the σ-power density curve of the M1-to-R phase transition as shown in Figure 4f. Actually, the appearance of the metastable M2 phase during the MIT is often observed [6], which complicates the actuator behaviors and leads to considerable hysteresis. Consequently, the M2-NW based micro-actuators are more controllable.

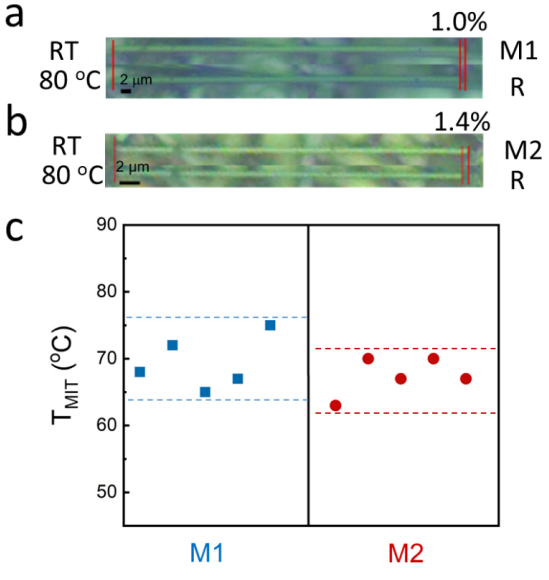

Figure S13 The length change and contrast change of the M1- and M2-phase NWs under the optical microscope are shown in (a) and (b), respectively. The T_{MIT} for the M1- (blue) and M2-phase (red) NWs in the heating process are shown in (c).

For pure, pristine VO_2 structures, T_{MIT} for the M2 phase is higher than that of the M1 phase. The value of T_{MIT} for the M2 phase can be as high as 100 °C under high tensile stress[7]. However, when the M2 phase is stabilized to room temperature by doping (Al, Cr et al.) or tuning the stoichiometry, the bias of the T_{MIT} for the M2 phase from the T_{MIT} for the M1 phase is insignificant compared to the stress effect. It is reported that the T_{MIT} for Al-doped M2 phase is slightly increased from TMIT for the M1 phase, depending on the Al concentration. In the case of highest Al concentration in their work, where x=0.025 in $V_{1-x}Al_xO_2$, the T_{MIT} is around 75 °C [8], near the T_{MIT} for the pristine M1 phase (T_{MIT} =68 °C). Similar phenomena are observed in Ga and Fe doped M2 phase [9]. The T_{MIT} for stoichiometric engineered M2 phase NWs is rarely reported. Prof. Lauhon et al. mentioned that the T_{MIT} for their M2-phase VO_{2+x} nanobeams is 68 °C [10], indicating the T_{MIT} is not dramatically influenced by the stoichiometry. Here, we carried out a premature experiment to verify the T_{MIT} for our M2-phase NWs. The VO_2 NWs grown on the silicon substrate are heated under the optical microscopes in air. The temperature is recorded by the heater. The phase transition is identified by the abrupt contrast change throughout the entire NW during the heating process. The NW length change across the MIT is quantitatively analyzed. The NWs whose length change goes beyond the theoretical value for the M1 phase (1%) are identified as the M2 phase, as shown in Figure S13 a and b. The measured T_{MIT} for multiple M1- and M2-phase NWs are displayed in Figure S13 c. No obvious change in the T_{MIT} is observed in our measurement, in consistence with the literature. However the measured T_{MIT} can be inaccurate, as the temperature of the NW on the silicon substrate may differ from the measured temperature. Experiments with specific equipment of precise temperature measurement and control in vacuum are needed to completely determine the T_{MIT} for the M2 phase.

Supplementary Movie ESM1 The *in situ* movie showing the phase evolution of the M2-phase NW displayed in Figure 4 as the current ramps up.

References

[1] Guo, H.; Chen, K.; Oh, Y.; Wang, K.; Dejoie, C.; Syed Asif, S. A.; Warren, O. L.; Shan, Z. W.; Wu, J.; Minor, A. M. Mechanics and dynamics of the strain-induced m1-m2 structural phase transition in individual VO_2 nanowires. *Nano Lett* **2011**, *11*, 3207-13.

[2] Hryha, E.; Rutqvist, E.; Nyborg, L. Stoichiometric vanadium oxides studied by xps. *Surface and Interface Analysis* **2012**, *44*, 1022-1025.

[3] Demeter, M.; Neumann, M.; Reichelt, W. Mixed-valence vanadium oxides studied by xps. *Surface Science* **2000**, *454-456*, 41-44.

[4] Liu, K.; Cheng, C.; Cheng, Z.; Wang, K.; Ramesh, R.; Wu, J. Giant-amplitude, high-work density microactuators with phase transition activated nanolayer bimorphs. *Nano Lett* **2012**, *12*, 6302-8.

[5] Tohmyoh; Hironori Heat conduction model for nanowire applications. *Applied Physics Letters 102*, 084107.

[6] Shi, R.; Cai, X.; Wang, W.; Wang, J.; Kong, D.; Cai, N.; Chen, P.; He, P.; Wu, Z.; Amini, A. et al. Single-crystalline vanadium dioxide actuators. *Advanced Functional Materials* **2019**, *29*, 1900527.

[7] Cao, J.; Gu, Y.; Fan, W.; Chen, L. Q.; Ogletree, D. F.; Chen, K.; Tamura, N.; Kunz, M.; Barrett, C.; Seidel, J. et al. Extended mapping and exploration of the vanadium dioxide stress-temperature phase diagram. *Nano Lett* **2010**, *10*, 2667-73.

[8] Strelcov, E.; Tselev, A.; Ivanov, I.; Budai, J. D.; Zhang, J.; Tischler, J. Z.; Kravchenko, I.; Kalinin, S. V.; Kolmakov, A. Doping-based stabilization of the m2 phase in free-standing VO_2 nanostructures at room temperature. *Nano Lett* **2012**, *12*, 6198-205.

[9] Brückner, W.; Gerlach, U.; Thuss, B. Phase diagram of $V_{1-x}Al_xO_2$. *Physica Status Solidi (a)* **1977**, *40*, K131-K134.

[10] Zhang, S.; Kim, I. S.; Lauhon, L. J. Stoichiometry engineering of monoclinic to rutile phase transition in suspended single crystalline vanadium dioxide nanobeams. *Nano Lett* **2011**, *11*, 1443-7.